



**HAL**  
open science

# Innovative design method and experimental investigation of a small-scale and very low-tip speed ratio wind turbine

M Bourhis, Michaël Pereira, Florent Ravelet, Ivan Dobrev

## ► To cite this version:

M Bourhis, Michaël Pereira, Florent Ravelet, Ivan Dobrev. Innovative design method and experimental investigation of a small-scale and very low-tip speed ratio wind turbine. 2021. hal-03182786v1

**HAL Id: hal-03182786**

**<https://hal.science/hal-03182786v1>**

Preprint submitted on 26 Mar 2021 (v1), last revised 23 Aug 2021 (v2)

**HAL** is a multi-disciplinary open access archive for the deposit and dissemination of scientific research documents, whether they are published or not. The documents may come from teaching and research institutions in France or abroad, or from public or private research centers.

L'archive ouverte pluridisciplinaire **HAL**, est destinée au dépôt et à la diffusion de documents scientifiques de niveau recherche, publiés ou non, émanant des établissements d'enseignement et de recherche français ou étrangers, des laboratoires publics ou privés.

# Innovative design method and experimental investigation of a small-scale and very low-tip speed ratio wind turbine

M. Bourhis<sup>a,\*</sup>, M. Pereira<sup>a</sup>, F. Ravelet<sup>a</sup>, I. Dobrev<sup>a</sup>

<sup>a</sup>Arts et Metiers Institute of Technology, CNAM, LIFSE, HESAM University, 75013 Paris, France

---

## Abstract

Small horizontal axis wind turbines operating at low wind speeds face the issue of low performance compared to large wind turbines. A high amount of torque is required to start producing power at low wind speed to overtake friction of mechanical parts. A low design tip-speed ratio ( $\lambda$ ) is suitable for low power applications. The relevance of the classical blade-element/ momentum theory, traditionally used for the design of large wind turbines operating at high tip-speed ratio, is controversial at low tip-speed ratio. This paper presents a new design methodology for a 300 mm horizontal axis wind turbine operating at very low tip-speed ratio. Chord and blade angle distributions were computed by applying the Euler's turbomachinery theorem. The new wind turbine has multiple fan-type blades and high solidity. The rotor was tested in wind tunnel and compared to a conventional 3-bladed horizontal axis wind turbine designed according to the classical blade-element/ momentum theory. It was found that the new wind turbine achieved a maximum power coefficient of 0.31 for  $\lambda = 1$ . The conventional wind turbine achieved similar performance but at higher tip-speed ratio  $\lambda = 3$ . At low tip-speed ratio, the torque coefficient ( $C_T$ ) is higher for the new wind turbine than for the conventional one and decreases linearly with the tip-speed ratio. The high magnitude of torque at low tip-speed ratio allows it to have lower instantaneous cut-in wind speed ( $2.4m.s^{-1}$ ) than the conventional wind turbine ( $7.9m.s^{-1}$ ). The analysis of the wake by stereoscopic particle image velocimetry shows that the new wind turbine induced a highly stable and rotating wake that could drive a second contra-rotating rotor. The magnitude of the axial and tangential velocities in the near wake shows a good correlation with the design requirements. Wake expansion and deceleration of the fluid are less significant with the new wind turbine than the conventional one.

*Keywords:* Small wind turbine, innovative design method, low tip-speed ratio, power and torque coefficients, stereo particle image velocimetry

---

## 1. Introduction

Wind is an inexhaustible resource. The conversion of the kinetic energy of the wind into mechanical or electrical energy useful for human activities has long been a source of concern. In fact, the first known wind power machine, a panemone windmill, was built in Persia from the 7<sup>th</sup> century b.c. for pumping water and grinding grain. Nowadays, academic research and engineering have made

possible the industrialization of large wind turbines able to generate several mega watts. Various classification of horizontal axis wind turbines are given in the literature [1, 2] but few are sufficiently accurate at small scale. A classification of wind turbines based on rotor diameter is proposed in Tab.1 in order to bring consistency to the discussion. Conventional large-scale horizontal axis wind turbines are well documented and spread over many territories. The main approach adopted by wind turbine manufacturers to design and analyse rotor blades is based on the blade-element/ momentum theory introduced by Glauert [3]. It combines the one-dimensional axial momentum theory introduced by Rankine and Froude and airfoil data to compute local force on a blade element. Assumptions and theoretical development are presented by Sørensen in Ref. [4] and some crucial results are given below. In the one-dimensional axial momentum theory the rotor has an infinite number of blades and the velocity of the fluid in the wake is purely axial which implies no rotation of the wake. For an incoming flow of air of density  $\rho$  with a freestream velocity  $V_\infty$ , the available power is  $P_a = \frac{1}{2}\rho\pi R_T^2 V_\infty^3$  where  $R_T$  is the radius of the rotor.

---

\*corresponding author

Email address: martin.bourhis@ensam.eu (M. Bourhis)

	Rotor diameter (m)	$\lambda$	$C_p$
Micro-scale	< 0.20	0 - 2	0.05 - 0.15
Centimeter-scale	0.20 - 0.50	2 - 5	0.20 - 0.35
Small-scale	0.50 - 5.0	4 - 8	0.35 - 0.50
Large-scale	> 5.0	6 - 9	0.40 - 0.50

Table 1: Classification of horizontal axis wind turbines based on rotor diameter. Power coefficient ( $C_p$ ) and tip-speed ratio ( $\lambda$ ) are the typical ranges in the literature

## Nomenclature

$\rho$	Density of the fluid	$\mu$	Dynamic viscosity	$V_\infty$	Free stream wind velocity
$N$	Number of blades	$Re$	Reynolds Number		
$dm$	Elementary mass of fluid	$d\dot{m}$	Elementary mass flow-rate		
$R_H$	Hub radius	$R_T$	Tip radius	$H$	Hub ratio
$a$	Axial induction factor	$c$	Chord	$\sigma$	Blade solidity
$\lambda$	Tip-speed ratio	$\lambda_r$	Local tip-speed ratio	$\omega$	Angular velocity
$r$	Radial coordinate	$z$	Axial coordinate		
$\alpha$	Angle of attack	$\varphi$	Rel. wind angle	$\beta$	Blade angle
$p_0$	Atmospheric pressure	$\Delta p$	Differential pressure	$T$	Temperature
$C$	Absolute velocity	$U$	Rotating velocity	$W$	Relative velocity
$C_p$	Power coefficient	$C_{p,max}$	Maximum power coefficient	$C_\tau$	Torque coefficient
$P_a$	Available power	$P$	Mechanical power	$\tau$	Torque
$C_D$	Drag coefficient	$C_L$	Lift coefficient	$C_F$	Resulting force coefficient
$C_N$	Normal load coefficient	$C_T$	Tangential load coefficient		
$\mathcal{U}$	Voltage	$\mathcal{I}$	Current intensity	$\mathcal{R}$	Electrical resistance
1	Upstream of the rotor	2	Downstream of the rotor		

The mechanical power produced by the wind turbine is  $P = \tau\omega$  with  $\tau$  the mechanical torque and  $\omega$  the angular velocity. The power coefficient  $C_p$  and the tip-speed ratio  $\lambda$  are defined as:

$$C_p = \frac{P}{P_a} = \frac{P}{\frac{1}{2}\rho\pi R_T^2 V_\infty^3} \quad (1)$$

$$\lambda = \frac{R_T\omega}{V_\infty} \quad (2)$$

According to the one-dimensional axial momentum theory, the rotor acts as a singularity which produces a pressure drop and a velocity defect in the wake. In the model, a constant discharge velocity in the rotor plane  $C$  is defined as  $C = V_\infty(1 - a)$  where  $a$  is the axial induction factor. Then the power coefficient associated to the power that can be extracted from the fluid reads  $C_p = 4a(1 - a)$ . By differentiating  $C_p$  with respect to  $a$ , the maximum power coefficient  $C_{p,max} = 16/27 \approx 0.59$  is obtained for  $a = 1/3$ . This results is commonly referred to as the Betz limit and states that no more than 59% of the available power could be transformed into mechanical power [5].

Glauert [3], Burton [6], Joukowski [7], Sørensen [4] and Wood [8] have proposed modified version of the one-dimensional axial momentum theory to design an optimum rotor while taking wake expansion, rotation and tip-losses into account in order to cope with the divergence of the chord at low tip-speed ratio ( $\lambda$ ) induced by the classical optimum rotor design. The maximum power coefficients for the proposed rotor models are quite similar and close to the Betz's limit at high tip-speed ratio  $\lambda$  but differ at low tip-speed ratio [4] where it tends to zero, contrary to the Betz's model which assumes a constant maximum power coefficient for the whole range of tip-speed ratio. Then, chord and pitch angle distributions are computed by applying the blade element theory. The following discussion is based on literature review and supported by Tabs. 1 & 2:

Je classe le tableau par taille en mm

Large-scale horizontal axis wind turbines usually operate at high tip-speed ratio, between 6 and 9, and achieves power coefficient of the order of  $C_p \simeq 0.5$ . At large-scale and high tip-speed ratio, the non-modified one-dimensional axial momentum theory combined with the blade element theory is adapted to design efficient wind turbines. The rotation of the wake induced by the rotation of the blades and the tip-losses have no significant impact on their performance because of their high operating tip-speed ratio and high dimension. Thus, chord and blade angle distributions computed with optimum rotor design method allowed wind turbines to achieve power coefficient equal to the predicted value given by the blade-element/ momentum theory.

Small-scale wind turbines, with a rotor diameter ranging from 0.5 m to 5 m achieves equal power coefficient in a quasi-equivalent range of tip-speed ratio (see Tab. 1) and are often designed using the same method as large-scale wind turbines (please see first part of Tab. 2). The prediction of the performance at this scale with the blade element/ momentum theory remains quite efficient. Some authors modified the classical blade-element/ momentum theory by applying correction factors that result in a change of the chord and blade angle distributions in order to match experimental and theoretical results. At small scale, some of them found a good agreement between experimental results and those predicted by the blade-element/ momentum [9, 12] and others suggested that the available experimental data were insufficient to evaluate the reliability of the theory [10] or obtained lower  $C_p$  than the expected value [16].

Centimeter-scale wind turbines and micro-scale wind turbines are designed to operate at low wind speed and for low power applications. By reducing the size of the rotor and the rated wind speed, the Reynolds number decreases and the reliability of the classical blade element/ momentum theory to design an efficient rotor becomes a controversial issue. Centimeter-scale wind turbines with a rotor diameter between 200 mm and 500 mm, designed ac-

Authors	Rotor diameter (mm)	Design Method	$N$	$\lambda_{design}$	$C_{p,max}$	$\lambda_{max}$
Elizondo <i>et al.</i> [9]	2900	BEM	3	-	0.40-0.45	6-7
Refan <i>et al.</i> [10]	2200	-	3	-	0.49	9
Singh <i>et al.</i> [11]	1260	BEM	2	6.6	0.29	6-7
Monteiro <i>et al.</i> [12]	1200	-	3	5	0.40	4.8
Lee <i>et al.</i> [13]	1000	BEM	3	5	0.469	5.61
Akour <i>et al.</i> [14]	1000	BEM	3	5	0.38	4.4
Abdelsalam <i>et al.</i> [15]	1000	BEM	3	4	0.426	5.1
Rotor diameter (mm)						
Nishi <i>et al.</i> [16]	500	BEM, tip chord = 0	3	5	0.240	5
	500	BEM, tip chord = 33.3mm	3	5	0.335	4.5
Hirahara <i>et al.</i> [17]	500	fan type, lin. chord, lin. twisted	4	3.3	0.4	2.7
Kishore <i>et al.</i> [18]	400	const. chord, non-lin. twisted	3	-	0.32	4.1
Kishore <i>et al.</i> [2]	394	lin. twist & tapering	3	-	0.14	2.9
Mendonca <i>et al.</i> [19]	200	BEM	3	3	0.29	3
Rotor diameter (mm)					Efficiency <sup>†</sup>	
Chu <i>et al.</i> [20]	120	Biomimetic design	3	-	0.087	3.2
Mendonca <i>et al.</i> [19]	100	BEM	4	1	-	1.2
Xu <i>et al.</i> [21]	76	Fan type	4	-	0.075	1.4
Rancourt <i>et al.</i> [22]	42	Fan type	4	-	0.095	0.8
Perez <i>et al.</i> [23]	40	-	4	-	0.058	0.75
Zakaria <i>et al.</i> [24]	26	Fan type	8	-	0.034	
Howey <i>et al.</i> [25]	20	Shrouded ducted type	12	1	0.09	0.6

Table 2: Summary of the literature review on small-scale and centimeter-scale wind turbines. BEM is the abbreviation for blade-element/momentum theory.  $\lambda_{design}$  is the designed tip-speed ratio and  $\lambda_{max}$  the tip-speed ratio related to  $C_{p,max}$ . <sup>†</sup>The efficiency given here is the ratio of the electrical power to the available wind power and is thus the product of  $C_p$  with unknown mechanical and electrical efficiencies

cording to the blade-element/ momentum theory achieve relatively low power coefficient —typically in the range  $0.20 \leq C_p \leq 0.35$  while operating at low tip-speed ratio  $2 \leq \lambda \leq 5$  as shown in Tab. 1, and second part of Tab. 2].

Finally, micro-scale wind turbines, with a diameter of the rotor lower than 200 mm, exhibit lower  $C_p$  in the range  $0.05 \leq C_p \leq 0.15$  and operate at very low tip-speed ratio  $0 \leq \lambda \leq 2$  [19–24]. At micro-scale, no author applied the classical blade-element/ momentum theory to design an optimum rotor and analyse their wind turbines. Under a certain Reynolds number, the flow regime becomes close to the laminar-turbulent transition and the aerodynamic properties of blade profiles differ from the ones obtained at high Reynolds number. The direct implementation of the blade-element/ momentum theory for the design of micro-scale and centimeter-scale wind turbines does not appear reliable for several reasons described below.

Firstly, they faces the issue of operating at low Reynolds number. Indeed, because of their small size and low operating wind speed, their profiles may undergo laminar separation bubble, a phenomenon that appears at the transition from the laminar to turbulent flow [26, 27]. The laminar flow detaches from the surface of the blade due to too high adverse pressure gradient that causes an increase of the size of the boundary layer and a loss of aerodynan-

mic lift. Large-scale wind turbines are not confronted to these issues because they operate at high Reynolds number where the boundary layers detachment is postponed to higher adverse pressure gradients. The choice of a particular airfoil also plays a major role in the aerodynamic performance of a wind turbine to avoid laminar separation bubble. A specific geometry can help to reduce the suction peak at the leading edge of the blade in order to prevent a too high adverse pressure gradient on the upper surface that can lead to separation of the flow at the surface. Thin profiles such as *SG60XX* series studied by Giguere and Selig [26, 28] show good performance at low Reynolds number. Some authors have reported performance improvement by increasing the leading edge nose radius, or by cusping the trailing edge [11]. A study performed by Lissaman *et al.* [29] stated that a small degree of roughness was associated with higher performance at low Reynolds number conditions.

Secondly, at small scale, wind turbines must generate enough torque to overtake friction losses between all mechanical parts even at low wind speed. As the mechanical power is equal to the product of torque times the angular velocity of the wind turbine, at a given power level, the higher the torque, the lower the angular velocity should be. Thus, at small scale, wind turbines should have low

rotating speed and therefore a low tip-speed ratio. From study of wind turbines in the same diameter range than the presented wind turbines, many authors concluded that a very low optimal tip speed ratio in the range of  $1 \leq \lambda \leq 3$  is suitable for small size rotors [17, 19, 21]. Indeed, for a given wind speed, the torque must be as high as possible in order to overtake the resistive torque of the mechanical parts contained in the nacelle and to start rotation and power production. The review on micro-scale wind turbines has shown that they operate at a very low tip-speed ratio  $0 \leq \lambda \leq 2$  (see bottom part of Tab. 2). In return, a high torque induces a high rotation of the fluid in the wake and significant losses. As mentioned before, the classical blade-element/ momentum theory for the design of wind turbine does not take into account the rotation of the wake, which has a significant impact at low tip-speed ratio. Then, various models that take into account the rotation of the wake have been proposed and are for instance presented in Ref. [4]. As a result, for tip-speed ratios in the range  $3 \leq \lambda \leq 6$ , the differences in pitch and chord distributions between the various models appear to be significant only in the inner 25% – 50% of the rotor. But for tip-speed ratio of the order of 1, the different models lead to significantly different designs of the blades from the root to the tip, with a dramatic increase of the chord distribution at the root for some of these models. Thus, as noticed by Sharpe [30], the solidity of the blade cascade could become as high as the assumption that the airfoils are isolated may no longer hold. Consequently, the reliability of the classical blade-element/ momentum theory for the design of an optimum rotor is still a controversial issue for wind-turbines operating at very low tip-speed ratio [4, 30].

Study on micro-scale wind turbines have shown other interesting results for the design of the 300 mm wind turbine presented in this paper. Leung *et al.* [31] compared various configuration of micro fan bladed wind turbine and concluded that multiblade and high solidity rotors (over than 50%) are suitable for micro scale wind turbines. Duquette *et al.* [32] also concluded that an increase of blade solidity and number of blades are associated with an increase of  $C_p$ . To summarize the literature review on micro-scale wind turbines, most of them have multiple fan-type blades, operate at low tip-speed ratio and have lower  $C_p$  than large-scale wind turbines [20–22, 24, 31].

Few authors worked on centimeter-scale wind turbines with a diameter between 200 mm and 500 mm. At this scale some authors tried to apply the blade-element/ momentum theory with various corrections and others presented chord and blade angle distribution based on the experience. Some results are presented in the central part of Tab. 2. Kishore *et al.* [18] designed a 3-bladed wind turbine with a diameter of 400 mm with a constant chord and non linearly twisted. They obtained a peak efficiency of 21%. Hirahara *et al.* [17] designed a 500 mm rotor linearly twisted and obtained a maximum power coefficient  $C_{p,max} = 0.4$  for  $\lambda = 2.7$ . Nishi *et al.* [16] manufac-

tured two 50 mm rotors according to the classical blade-element/momentum theory with Prandtl’s tip loss factor but with different tip chord length. They obtained a 38.7% higher  $C_{p,max}$  with the increase of the tip chord length. However, these studies present wind turbine with high design and optimum tip-speed ratio where the classical blade-element/ momentum theory give quite efficient results. To the best of our knowledge, no design method for a centimeter-scale wind turbine operating at very low tip-speed ratio has already been submitted because of the controversial design and low performance given by the blade-element/ momentum theory.

Thus, the aim of this study is to introduce an innovative design method for a 300 mm horizontal-axis wind turbine that operates at very low tip-speed ratio. In order to compare the behaviour of the innovative wind turbine, a 300 mm and 3 bladed horizontal-axis wind turbine was designed according to the classical blade-element/ momentum theory. Both methods are described in § 2. A detailed investigation of the performance of both wind turbines were performed. Moreover, stereoscopic particle image velocimetry processing were carried out in order to examine and compare the wake behind both wind turbines. The experimental apparatus are presented in § 3. Finally, the results are presented in § 4 and discussed in § 5.

## 2. Design Methods

Two small-scale wind turbines were designed with two different methods. The first one is based on the blade-element/ momentum theory and the other relies on the Euler’s turbomachine equation traditionally used for the design of pumps and turbines. Both wind turbines were designed with the same design brief in order to compare their special features. For the design, air with  $\rho = 1.2 \text{ kg.m}^{-3}$  and  $\mu = 1.8 \times 10^{-5} \text{ Pa.s}$  was considered as the working fluid. The design free stream wind velocity was set at  $V_\infty = 10 \text{ m.s}^{-1}$ . The selected rotor radius and hub radius were respectively set at  $R_T = 150 \text{ mm}$  and  $R_H = 45 \text{ mm}$ . The hub ratio  $H = \frac{R_H}{R_T}$  is thus equal to 0.3 for both wind turbines. In both design methods, the following equations from the classical one-dimensional axial momentum theory were used:

$$C = (1 - a)V_\infty \quad (3)$$

$$C_p = 4a(1 - a)^2 \quad (4)$$

To maximize power extraction from the fluid, the design axial induction factor was set at  $a = 1/3$  that corresponds to the Betz’s limit  $C_p \simeq 0.59$ . The predicted power output from the wind turbine is  $P \simeq 25.1 \text{ W}$  according to Eqs. 1& 4. Chord and angle distributions are computed in two distinct ways, by applying either the Euler’s theorem or the blade-element theory. For easier reading, the wind turbine designed according to the blade-element/ momentum theory is named BWT and the other, designed by applying the Euler’s theorem, is the EWT.

## 2.1. BWT design method

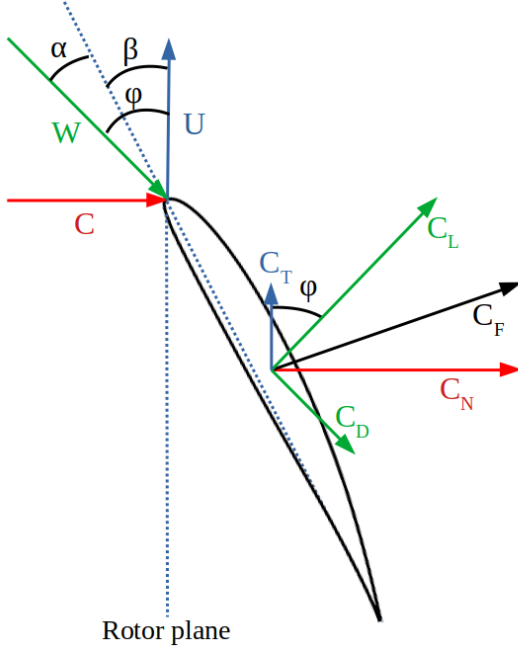


Figure 1: Velocity triangle and projections of the aerodynamic coefficients on the on the SG6042 airfoil

A conventional three-bladed wind turbine was designed with a tip-speed ratio  $\lambda = 3$ . Chord and pitch angle distributions were computed according to the classical blade-element/ momentum theory without any corrections. The blade was discretized in 11 sections from root to tip where local chord and pitch angle were computed. The local blade pitch angle  $\beta(r)$ , that is the angle between the chord line and the rotation plane was calculated with the velocity triangle (see Fig. 1), using Eqs. 5& 6:

$$\varphi(r) = \arctan\left(\frac{C}{U(r)}\right) \quad (5)$$

$$\beta(r) = \varphi(r) - \alpha \quad (6)$$

In equations 5& 6,  $\varphi$  is the angle between the relative velocity and the rotation plane,  $C$  is the axial velocity in the rotor plane,  $U$  is the rotation speed of the rotor and  $\alpha$  is the angle of attack between the relative velocity and the chord line. The chord  $c$  is computed using Eqs. 7 to 9, in which  $C_L$  and  $C_D$  are the lift and drag coefficients at the angle of attack  $\alpha$  and  $\sigma$  is the local blade cascade solidity, defined as the ratio of the blade chord length to the azimuthal pitch distance.

$$C_N = C_L \cos(\varphi) + C_D \sin(\varphi) \quad (7)$$

$$\sigma(r) = \frac{4a \sin^2(\varphi)}{(1-a)C_n} \quad (8)$$

$$c(r) = \frac{2\pi r \sigma(r)}{N} \quad (9)$$

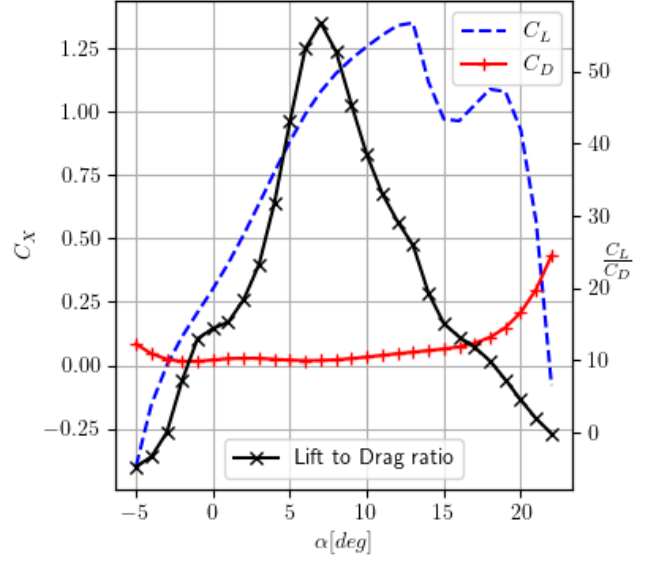


Figure 2: Digitized SG6042 polar plots for  $Re = 10^5$  according to Ref. [33]

The SG6042 airfoil was selected because of the high lift-to-drag performances at low Reynolds number [26, 28]. This airfoil is widely used for small-scale wind turbines. The polar plot of SG6042 airfoil was digitised in order to obtain lift and drag coefficients for the optimum angle of attack  $\alpha = 6^\circ$  (Fig.2). As mentioned in the introduction, a very low tip-speed ratio seems to be inappropriate for the design of this turbine. Indeed, a decrease of  $\lambda$  induces an increase of the relative wind angle  $\varphi$  (Eq. 5) and thus an increase of the blade pitch angle and solidity (Eq. 8). The lift and drag coefficients that are used in the blade-element theory are obtained from isolated and two-dimensional airfoils data. Wind turbine design parameters are summarized in Tab. 3 and plots of chord length, blade pitch angle and blade solidity are presented in Fig. 4a, 4c. The chord length is varying from 82 mm at the root to 30 mm at the tip with an average chord length of 45 mm. The blade is non-linearly twisted and the pitch angle decreases from  $31^\circ$  to  $6.5^\circ$ . Reynolds number  $Re(c_{avg})$   $Re(c_{tip})$  are computed according to:

$$Re(r) = \frac{\rho W(r)c(r)}{\mu} \quad (10)$$

with  $c_{tip} = c(R_T)$ ,  $c_{avg} = c(R_T/2)$  and  $W$  the relative velocity.

## 2.2. Euler's design method

The design method relies on the Euler's turbomachine equation. Micro-scale and centimeter-scale wind turbines need a high starting torque to produce power at low wind speed by overtaking friction torque of the different mechanical parts. To achieve this purpose, a low tip-speed

ratio and multi-bladed wind turbine is suitable [17, 19, 21]. As mentioned in the previous section, a decrease of the tip-speed ratio is associated with uncertainties on aerodynamic coefficients. The new design method freed from airfoils data. The main purpose is to force the geometric deflection of the fluid due to the shape of the blade in order to generate the designed power  $P$ . Thus a high blade solidity and a significant number of blades are required to constrain the fluid into the blade cascade arrangement. On this basis, the EWT was designed with a tip-speed ratio  $\lambda = 1$ , has 8 blades and one imposes a high solidity at the root and tip of the blades, respectively  $\sigma(R_H) = 1.65$  and  $\sigma(R_T) = 0.7$ . The Euler's turbomachinery equation *i.e* the angular momentum balance is applied on an annular disc of turbines at radii  $[r, r + dr]$ . The angular momentum balance reads:

$$d\tau = d\dot{m}(C_{\theta 2}r - C_{\theta 1}r) \quad (11)$$

where  $d\tau$  is the elementary torque applied by the rotor on the fluid,  $C_\theta$  the tangential speed of the fluid and  $d\dot{m}$  the elementary mass flow-rate. The index 1 refers to upstream of the rotor and 2 downstream of it. One assumed an axial upstream wind speed  $C_1 = V_\infty(1 - a)$ , therefore  $C_{\theta 1} = 0$ . The elementary mass of fluid that goes through the annular disc between times  $t$  and  $t + dt$  is  $dm = \rho 2\pi r dr C_1 dt$ . The associated elementary mass flow-rate is  $d\dot{m} = \rho 2\pi r dr C_1$ . The elementary power transferred from the fluid to the rotor is obtained by multiplying the previous equation by the angular rotating speed of the ro-

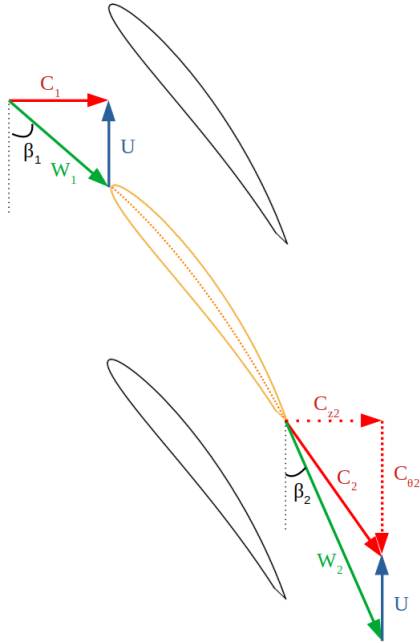


Figure 3: Blade cascade and velocity triangle for the EWT. Index 1 refers to upstream of the rotor and 2 downstream of it.  $U$  is the rotating velocity of the rotor,  $W$  the relative velocity in the turbine's reference frame and  $C$  the absolute velocity.

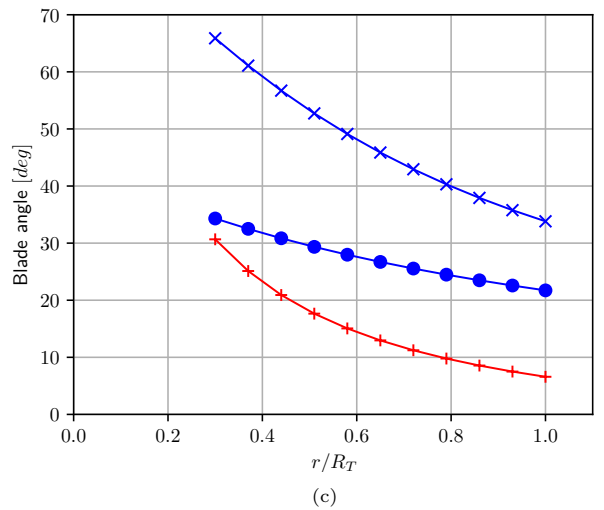
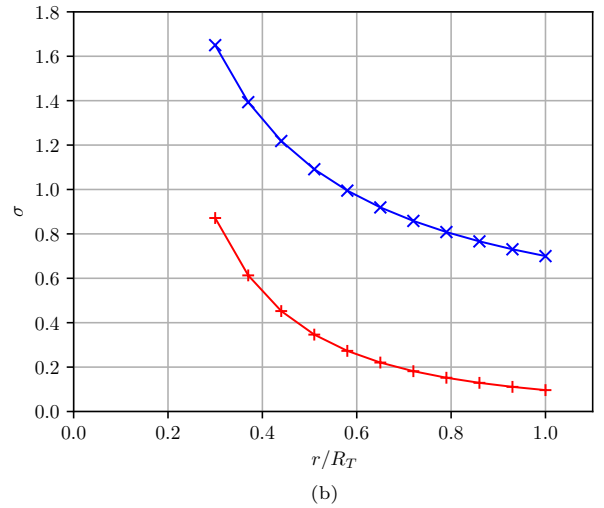
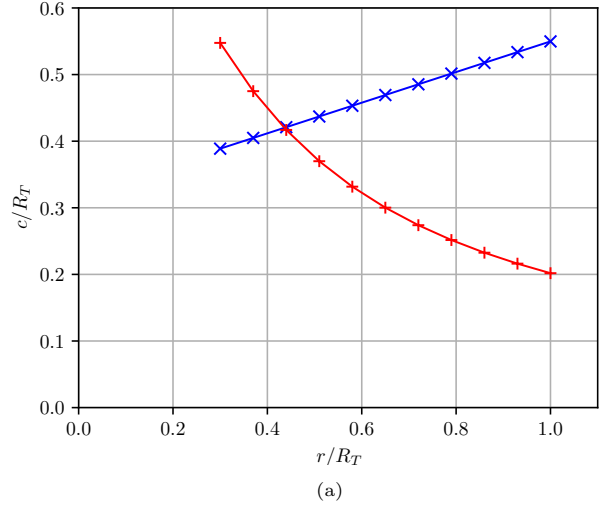


Figure 4: Geometry distributions as a function of normalized radial coordinate for the EWT ( $\times$ ) and for the BWT ( $+$ ). (a): chord length; (b): blade solidity  $\sigma = \frac{Nc}{2\pi r}$  and (c): pitch angle  $\beta$  for the BWT (Fig.1) and blade angles at the input  $\beta_1$  ( $\times$ ) and output  $\beta_2$  ( $\bullet$ ) of the EWT (Fig.3)

tor.

$$dP = d\dot{m}C_{\theta 2}U_2 \quad (12)$$

By integrating on the whole span :

$$P = \int_{R_H}^{R_T} d\dot{m}C_{\theta 2}U_2 \quad (13)$$

$$P = 2\pi\rho(1-a)V_{\infty}\omega \int_{R_H}^{R_T} r^2 C_{\theta 2} dr \quad (14)$$

If ones assumed a constant tangential velocity  $C_{\theta 2}$  :

$$P = 2\pi\rho(1-a)V_{\infty}\omega C_{\theta 2} \int_{R_H}^{R_T} r^2 dr \quad (15)$$

$$P = 2\pi\rho(1-a)V_{\infty}\omega C_{\theta 2} \left[ \frac{R_T^3}{3} - \frac{R_H^3}{3} \right] \quad (16)$$

Therefore, the tangential velocity of the fluid downstream the rotor is given by :

$$C_{\theta 2} = \frac{P}{2\pi\rho(1-a)V_{\infty}\omega \left[ \frac{R_T^3}{3} - \frac{R_H^3}{3} \right]} \simeq 6.8 \text{m.s}^{-1} \quad (17)$$

The tangential velocity of the fluid must be equal to  $6.8 \text{m.s}^{-1}$  to obtain the desired power  $P$ . The velocity triangle allows the computation of the blade angles at the input and output of the rotor (Fig. 3).

$$\beta_1 = \arctan\left(\frac{V(1-a)}{r\omega}\right) \quad (18)$$

$$\beta_2 = \arctan\left(\frac{V(1-a)}{C_{\theta 2} + r\omega}\right) \quad (19)$$

One imposes a linear chord distribution, computed according to Eq. 9, that meets blade solidity conditions at root and tip. Thus the chord length is varying linearly from 58 mm at the root to 82 mm at the tip with a mean chord length of 70 mm. Wind turbine design parameters are summarized in Tab. 3 and plots of chord length, pitch angle and blade cascade solidity are presented in Figs. 4c, 4a. Both wind turbines operate at low Reynolds number compared to large-scale wind turbines. The flow regime is closed to the laminar-turbulent transition at which viscous effect can alter aerodynamic properties of airfoils and wind turbine performance. CAD pictures of the two wind turbines are moreover available in Fig. 5.

### 3. Experimental setup

In order to investigate experimentally the wind turbines performance, both prototypes were manufactured by stereolithography to obtain an equal degree of roughness.

#### 3.1. Performance

The performance of both wind-turbines were evaluated in terms of power coefficient  $C_p$  and torque coefficient  $C_{\tau} = \frac{C_p}{\lambda}$  for various tip-speed ratios. The experimental study is carried out in the wind tunnel of the *LIFSE* facilities. The Prandtl type wind tunnel has an axial fan with a rotor diameter of 3 m controlled by an asynchronous motor. Behind the fan, the flow is decelerated and straightened in a settling chamber equipped with honeycomb strenghteners. Upstream of the test section, the flow is accelerated by means of a tunnel nozzle with a contraction ratio of 12.5. The test section has a cross-section  $1.35 \times 1.65 \text{m}^2$  and is 1.80 m long. The turbine was mounted on an 530 mm tall mast with a 700 mm long nacelle containing a rotating shaft on which a DC motor MAXON, used as a generator, and a rotating torque meter HBMTW20 were anchored. The contactless torque transducer with range 2 N.m and accuracy of 0.002 N.m ensured the coupling between the rotor shaft and the generator. Moreover, it delivers 360 pulses per revolution and thus allows angular velocity measurement. The generator was wired to resistors and used as a brake system by imposing a resistive torque to the wind turbine. Characteristics of the generator  $\mathcal{U} = f(\omega)$  and  $\mathcal{I} = f(\tau)$  were previously determined. The voltage at the generator terminals is proportional to the angular velocity of the shaft for  $0 \text{V} \leq \mathcal{U} \leq 35 \text{V}$  according to  $\mathcal{U} = 0.124\omega$  with a coefficient of determination  $R^2 = 0.9975$ . The electrical current through the resistance varies with the torque according to  $\mathcal{I} = 8.27\tau - 0.23$  with a coefficient of determination  $R^2 = 0.9955$ . The residual torque at zero current is a measure of the friction torque of the bearings placed between the torque transducer and the generator. The static torque was systematically measured and removed from acquisitions but frictionnal losses in the bearing have not been included in the computation of the power coefficient. The atmospheric pressure  $p_0$  and temperature  $T$  were consistently recorded before acquisition in order to evaluate air density  $\rho = \frac{p_0}{rT}$  with  $r$  the specific gas constant for air. Wind speed was calculated with the measurement of the relative pressure *via* a Pitot probe placed in the wind tunnel  $V_{\infty} = \sqrt{\frac{2\Delta p}{\rho}}$ .

The wind speed in the tunnel is kept approximatively constant at  $V_{\infty} = 10 \text{m.s}^{-1}$  whereas the resistive torque on the wind turbine will be modified between each acquisition by changing the voltage to the generator. All acquisitions were made at constant resistive load on the generator. The signals of  $T$ ,  $\Delta p$ ,  $\tau$  and  $\omega$  were recorded at a sampling frequency of 1000 Hz and digitized using an NI USB6229 acquisition card. For various resistive load, 50 samples of 0.5s were acquired and for every samples, the means of  $T$ ,  $\Delta p$ ,  $\tau$  and  $\omega$  were logged in a file text. A change of the sampling frequency or time acquisition have shown any significant differences. Then, for all acquisitions, the means and standard deviations of electrical quantities were computed and converted to physical values by applying the



Figure 5: CAD of the EWT and BWT

	$R_T(mm)$	$P(W)$	$H$	$a$	$\lambda$	$N$	Airfoil	$\alpha(^{\circ})$	$\sigma(R_H)$	$\sigma(R_T)$	$Re(c_{avg})$	$Re(c_{tip})$
BWT	150	25.13	0.3	1/3	3	3	SG6042	6	0.87	0.10	61900	62000
EWT	150	25.13	0.3	1/3	1	8	NACAxx10	x	1.65	0.70	43800	66200

Table 3: Wind turbines design parameters

conversion factor of each measurement machine preliminarily determined experimentally.

### 3.2. Wake analysis by stereoscopic particle image velocimetry

The stereoscopic particle image velocimetry (stereo-PIV) is handled by DynamicsStudio, a software edited by Dantec. The stereo-PIV system is equipped with a Nd-Yag laser of wavelength 532 nm (Litron Nano-L 200-15) with an impulse power of 200 mJ. The cameras for pictures acquisitions have a resolution of  $2048 \times 2048$  pixels and are supplied with a lens (Micro-Nikkor AF 60 mm f/2.8D), a frame grabber card and a synchronization system. A Scheimpflug system is coupled to the cameras in order to make colinear the plane of interest behind the rotor, the lens plane and the image plane. The flow was continuously seeded with 2 to 5  $\mu\text{m}$  diameter drops of oil swarmed by a fog machine. The particle tracers were illuminated twice by a light sheet within the flow generated by the laser. The position and angular position of the laser was previously adjusted in order to make the laser sheet and plane of rotation of the rotor coincide. The delay between two pulses was set at 100  $\mu\text{s}$  in order to get a tracer's displacement of approximately a quarter of the length of the interrogation window. The coupled Scheimpflug cameras were used for images acquisition and triggered by the laser firing. Approximately 200 double frame images were acquired with each wind-turbine mounted and operating at their optimum tip-speed ratio. After image dewarping and applying of the calibration, the local displacement vector for the images of the tracer particles of the first and second illumination was computed for each interrogation window

by adaptiv-correlation. Then the three components of the local flow velocity into the plane of the light sheet were reconstructed by stereo-particle image velocimetry processing. Theoretical and practical developments of the particle image velocimetry are presented by Raffel *et al.* [34]. The origin of the physical frame is located at the intersection of the rotor axis and the plane of blade's leading edge. Two sets of acquisitions were conducted with different acquisition mode. Laser firing and image acquisition were first synchronized with the blade angular position. One image was acquired at every passage of a same blade at a vertical position. Results from these acquisitions are named synchronized acquisitions. A second set of acquisitions were performed during which laser firing and pictures acquisitions were triggered by an internal clock set at 2 Hz. This triggering mode allows the acquisition of images for various angular position of the rotor. By acquiring 200 double frame images, the velocity fields are computed by doing a simple mean on the whole azimuth for each velocity components. Results from these acquisitions are named non-synchronized acquisitions. Stereo-PIV acquisitions were acquired for both wind turbines operating at their optimum tip-speed ratio.

## 4. Results

### 4.1. Performance analysis

In this section, comparisons between the experimental results obtained from the two rotor designs are presented and discussed. Experimental plots of  $C_T(\lambda)$  are presented in Fig. 6a. The starting torque coefficient *i.e.*  $C_T(\lambda = 0)$  of

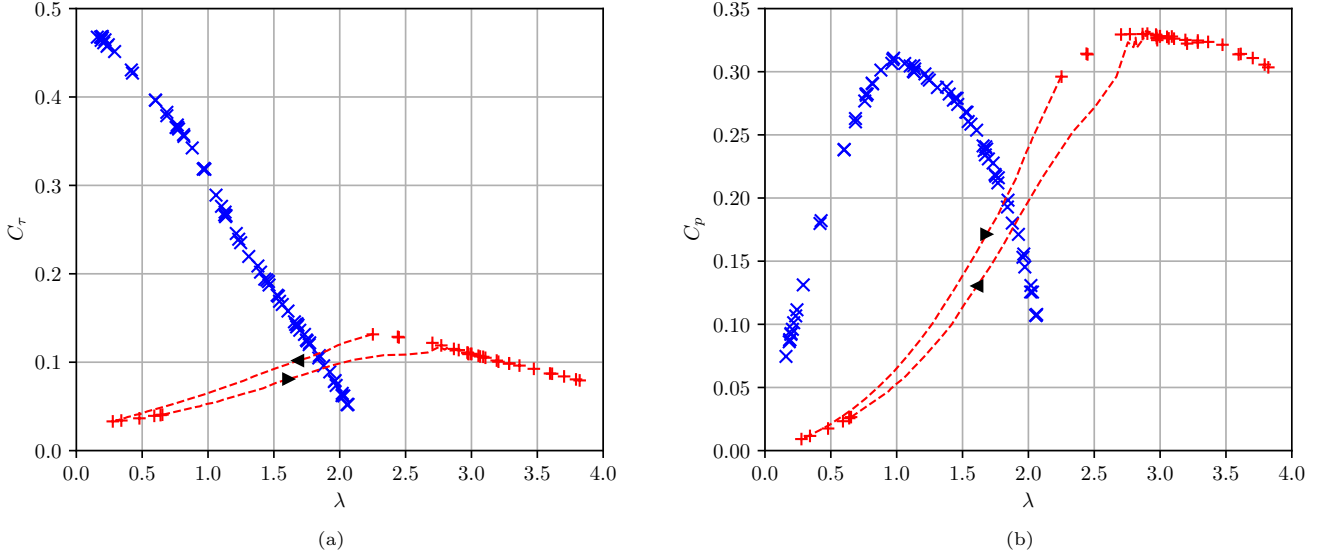


Figure 6: Torque coefficient  $C_T$  (a) and power coefficient  $C_p$  (b) as a function of tip-speed ratio  $\lambda$  for the BWT (+) and for the EWT ( $\times$ ). Both experimental plots were obtained with a free stream wind velocity  $V_\infty = 10\text{m.s}^{-1}$ . The BWT present transient periods (---) that depend on the direction of variation of  $\lambda$  ( $\blacktriangleright$ )

the EWT is equal to 0.523. For comparison the starting torque coefficient of the BWT is equal to  $C_T = 0.03$ . As the ratio of the EWT starting torque to the BWT starting torque is approximately equal to 16, the EWT will generate the same torque at  $\omega = 0$  with 4 times lower wind speed than the BWT. The cut-in wind speed of both wind turbines were measured in order to compare their behaviour at very low wind speed. For this purpose, the resistor was disconnected from the generator and the wind speed was gradually increased. The instantaneous cut-in wind speed was defined as the speed at which the wind turbine begins to rotate without stopping and without manual intervention. Thus, the wind turbine must overtake the friction torque of the mechanical parts contained in the nacelle. The cut-in wind speed was measured at  $2.4\text{m.s}^{-1}$  for the EWT and  $7.9\text{m.s}^{-1}$  for the BWT. The ratio of the cut-in wind speed is in the same order of magnitude as the starting torque ratio.

The EWT's torque coefficient decreases linearly with the tip-speed ratio according to  $C_T = -0.226\lambda + 0.523$  with a coefficient of determination  $R^2 = 0.9979$ . The EWT is able to operate in a wide range of torque, from  $C_T = 0.523$  at  $\lambda \approx 0$ , to  $C_T = 0.05$  at  $\lambda = 2$ . For comparison, the maximum torque coefficient of the BWT is  $C_T = 0.126$  and occurs at the tip-speed ratio  $\lambda = 2.3$ . Its range of  $C_T$  is limited from 0.03 at  $\lambda \approx 0$  to its maximum value. Moreover, for the BWT, one can notice that no steady experimental data points are displayed in the  $C_p(\lambda)$  and  $C_T(\lambda)$  curves in the range  $0.7 \leq \lambda \leq 2.3$ . This is due to the fact that the torque as a function of the angular velocity does not behave monotonically: the torque coefficient of the BWT first increases with  $\lambda$  from  $\lambda = 0$  to  $\lambda \simeq 2.3$

and then decreases. Thus, there is a range of corresponding  $\lambda$  for which the characteristic curve  $\mathcal{U} = f(\mathcal{I})$  of the generator with the BWT mounted on it does not presents intersection point with the characteristic curve of the load  $\mathcal{U} = \mathcal{R}\mathcal{I}$  for the associated range of resistive load. Thus, with the present direct coupling of the DC generator to a resistive load, there is an unstable branch for the BWT: the system skips from an operating point at one end of the first branch to another operating point on the second branch in a transient way. Torque and angular velocity were measured during two transients and the paths that have been followed in the phase space of the system are displayed with dashed lines in Fig. 6. The blacktriangles ( $\blacktriangleright$ ) indicate the direction of variation of the curve. The path between two stable operating points differs under the increases/decreases of the load *i.e* the decreases/increases of the tip-speed ratio. The duration of the transient depends on the mechanical inertia of the system and is here of the order of a few hundreds of seconds. Moreover, for a given torque coefficient  $C_T$ , the BWT presents several operating points corresponding to different values of  $\lambda$ . One operating point is stable and the two others, located on the transient curves, are unstable and lead to an acceleration or a deceleration of the wind turbine until a stable regime is eventually restored. Thus, with a voltage regulation by a resistor or a resisting torque control strategy, the BWT cannot operate in the whole range of tip-speed ratios.

On the contrary, the EWT has a single  $\lambda$  and thus a unique operating point for its whole range of torque coefficient. Moreover, the steep  $C_T(\lambda)$  curve of the EWT compared to the BWT is remarkable and could be useful for electrical applications. Indeed, the EWT can run for a

wide range of load and presents a linear response of its angular velocity to a voltage regulation. These advantages could be favorable to charge a battery where a sensitive adjustment of the angular velocity is required in order to maintain it and the charging voltage constant.

The power coefficient  $C_p$  of both wind turbines were also compared for various tip-speed ratio. Experimental results of  $C_p$  are presented in Fig.6b. The maximum power coefficient of the EWT is  $C_{p,max} = 0.31$  and is obtained for  $\lambda = 1$ , that corresponds well to the designed tip-speed ratio. The associated mechanical power is  $P = 13.1W$ . The maximum power coefficient of the BWT is  $C_{p,max} = 0.33$  and is obtained for  $\lambda = 2.9$ . Such as reported in [16], the maximum power coefficient is lower than the predicted value by the blade-element/ momentum theory but the optimum tip-speed ratio corresponds well to the designed tip-speed ratio. The maximum mechanical power generated by the BWT is  $P = 14.0W$ . Few studies reported such good performance for this size of wind-turbine. Moreover, most of wind turbines with a diameter between 200 and 500 mm are designed for a tip-speed ratio close to 3 and have equal or fewer power coefficient [2, 16–19]. To the best of our knowledge, the EWT is the first wind turbine designed to operate at  $\lambda = 1$  that achieved such performance at this scale.

#### 4.2. Wake analysis

The tangential and axial velocity fields and profiles for both wind turbines are respectively presented in Figs. 7 and 8. The left column corresponds to the results obtained for the EWT and the right column to the results of the BWT. Synchronized acquisitions show, in particular, the locations of the wingtip vertices and the spiral form of the vortex in the wake.

Tangential velocity fields in Figs. 7a, 7c and profiles in Fig. 7e] for the EWT show high magnitude of tangential velocity in the wake of the EWT from  $10 \text{ m.s}^{-1}$  at a distance of  $2R_T/3$  at the level of the hub to  $6.5 \text{ m.s}^{-1}$  at a distance of  $5R_T/3$ . Moreover, the tangential velocity magnitude in the vortex center was measured and decreased with distance from the wind turbine:  $C_{\theta 2} = 6.8 \text{ m.s}^{-1}$  at  $z = 111 \text{ mm}$  for the first center,  $C_{\theta 2} = 5.6 \text{ m.s}^{-1}$  at  $z = 190.5 \text{ mm}$  for the second center and  $C_{\theta 2} = 4.8 \text{ m.s}^{-1}$  at  $z = 267.8 \text{ mm}$  for the last one. The wake angle, defined as the angle between the rotor axis and a straight line joining vertices's centers is approximately equal to  $3^\circ$ . An equal angle is obtained from non-synchronized acquisition. The radial distance between the vortex and the rotor axis decreases by 2 mm for each center. These indicators characterize wake's expansion behind the EWT. Moreover, the axial distance between each center of vortex decreases from  $d = 79.6 \text{ mm}$  to  $d = 77.3 \text{ mm}$  which corresponds to a decrease in the length of the spiral form of vortex. Furthermore the EWT was designed with an expected tangential speed of  $6.8 \text{ m.s}^{-1}$  in the wake in order to generate the desired power  $P$ . The assumption of a constant tangential velocity along the span made for the design of the EWT

seems incorrect according to Fig. 7e. However, the results presented in Tab. 4 indicate that the average tangential velocity along the span, *i.e* for  $r \in [45; 150] \text{ mm}$ , are closed to the designed tangential speed for various distance from the physical frame origin. The tangential velocity profiles for various distance from the EWT are very similar from root to tip. A linear interpolation from the tangential velocity profile at the distance  $z = R$  from the wind turbine was conducted. It shows that the tangential velocity decreases linearly from root to tip as follows:  $C_{\theta 2} = -0.045r + 10.402$  with a coefficient of determination  $R^2 = 0.9992$ . This discovery could be useful for the design of a new prototype with a linear expression of  $C_{\theta 2}$  rather than a constant one as assumed in the design method. The high magnitude of tangential velocity in the wake is associated with high energy losses in the rotating wake. This kinetic energy could be recovered by a contra-rotating wind turbine placed behind the EWT. Based on the design method presented in this paper, the contra-rotating wind turbine could be design with a linear expression of the tangential upstream wind speed  $C_{\theta 1,CR} = C_{\theta 2}$  and a tangential downstream velocity equal to zero  $C_{\theta 2,CR} = 0$  in order to straighten fluid streamlines and mitigate wake expansion.

The shape of axial velocity profiles of the EWT are almost similar for various distance  $z$  from the origin (see Fig. 8e). The axial speed in the wake along the span of the blade is relatively constant and equal to  $C_{\theta 2} = 6.5 \text{ m.s}^{-1}$ . As made before for the tangential velocity, the simple mean of the axial velocity along the span for several distance from the origin is presented in Tab.5. From the results of the mean of the axial velocity, the axial induction factor is calculated according the equation:

$$\langle a \rangle = \frac{V - \langle C_{z2} \rangle}{V}$$

An axial induction factor equal to  $a = 0.33$  was set for the design of both wind turbines. The experimental measurements of axial induction factor vary from  $a = 0, 339$  at  $z = R_T/3$  to  $a = 0.330$  at  $5R_T/3$  and show low magnitude of variation. Results are really closed to the design settings that proved the good efficiency of the design method.

For comparison, a similar study was conducted with the BWT. Tangential velocity fields (see Fig. 7b, 7d) and profiles (Fig. 7f) from the BWT show low magnitude of tangential velocity in the wake of the BWT. The profile for a distance of  $R_T/3$  show high variation near the root of the blade and is barely explainable. The tangential velocity profiles for various distances show a high degree of similarity. Along the span, the maximum magnitude of tangential velocity is approximately  $1.5 \text{ m.s}^{-1}$ . The measure of the tangential speed in vortex centers show a decrease from  $1.99 \text{ m.s}^{-1}$  for the first center to  $1.30 \text{ m.s}^{-1}$  for the last one. The distance between each center varies from  $82.6 \text{ mm}$  to  $75.7 \text{ mm}$ . Moreover, the distance from the axis of rotation is growing linearly from  $z = 162.6 \text{ mm}$  for the first center to  $z = 179.45 \text{ mm}$ . The wake angle is approx-

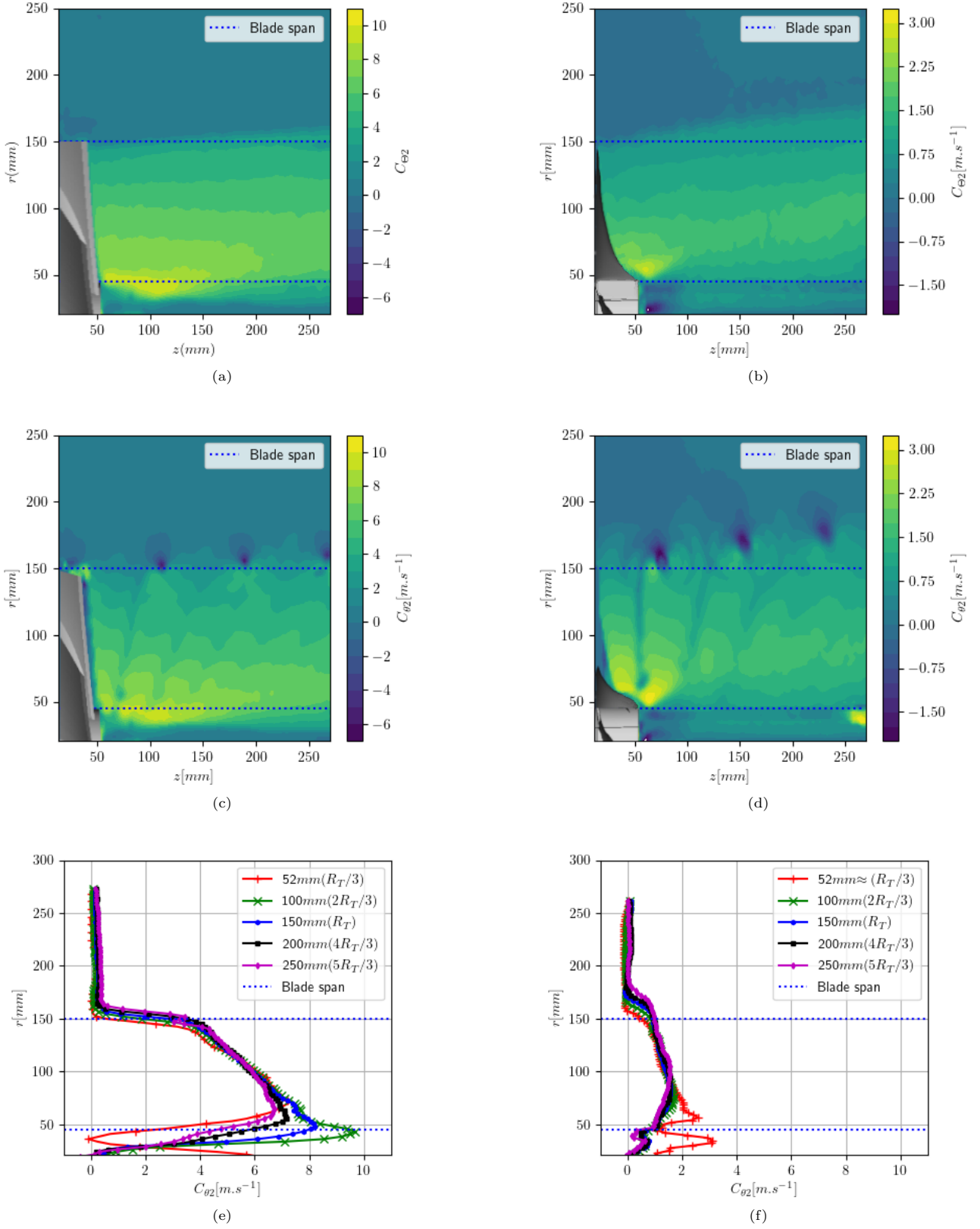


Figure 7: **Tangential velocity fields and profiles from stereo-PIV acquisitions.** On the left side of the page, the EWT was operating at ( $\lambda = 1; V_{\infty} = 10\text{m.s}^{-1}$ ) and on the right side, the BWT at ( $\lambda = 3; V_{\infty} = 10\text{m.s}^{-1}$ ). (a, b) : Non-synchronized acquisitions. (c, d) : Synchronized acquisitions. (e, f) : Tangential velocity profiles derived from non-synchronized acquisitions for various distance  $z$ . The reference frame origin is located at the intersection of the rotation axis with the blade leading edge

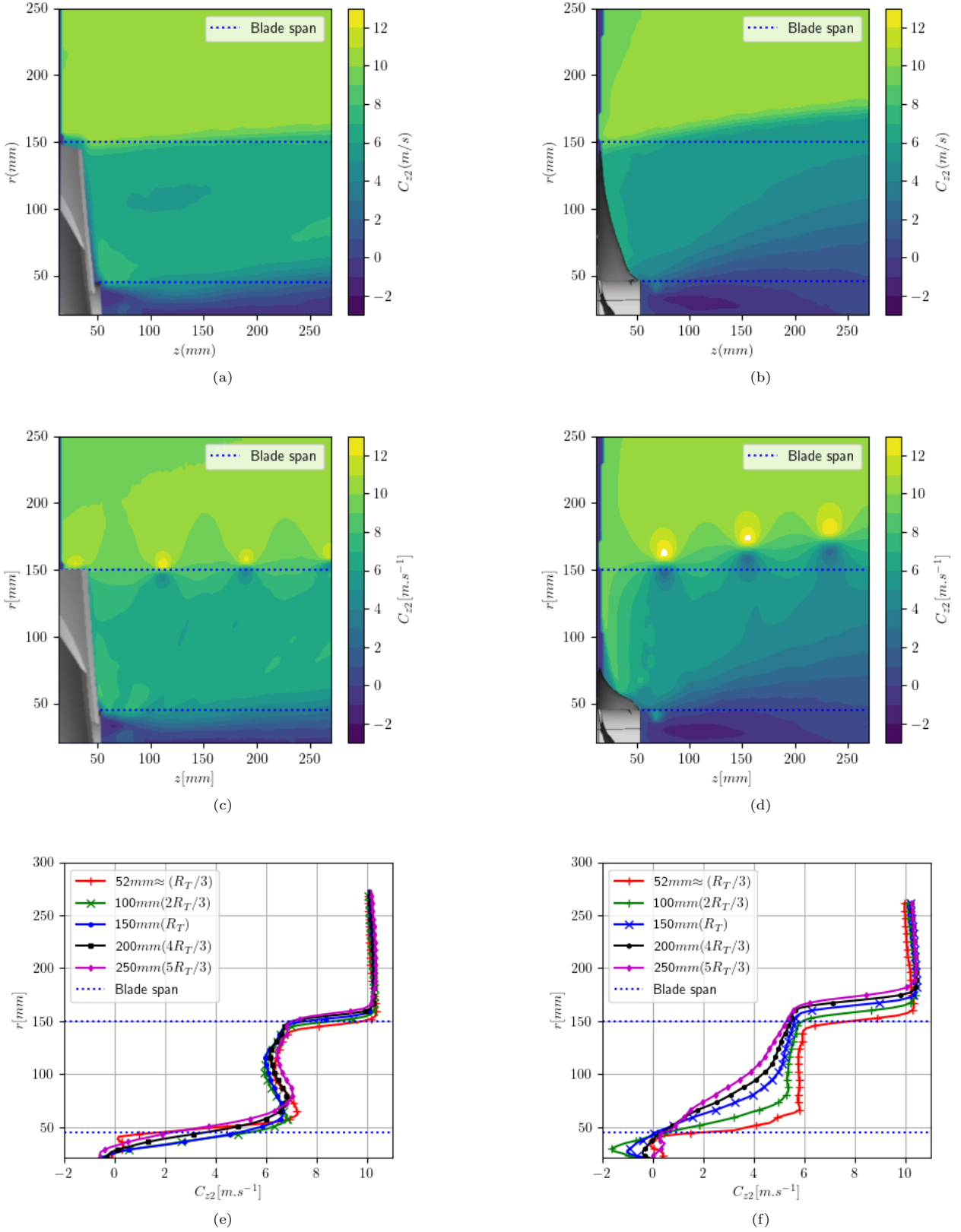


Figure 8: **Axial velocity fields and profiles from stereo-PIV acquisitions.** On the left side of the page, the EWT was operating at ( $\lambda = 1; V_\infty = 10m.s^{-1}$ ) and on the right side, the BWT at ( $\lambda = 3; V_\infty = 10m.s^{-1}$ ). (a, b) : Non-synchronized acquisitions. (c, d) : Synchronized acquisitions. (e, f) : Tangential velocity profiles derived from non-synchronized acquisitions for various distance  $z$ . The reference frame origin is located at the intersection of the rotation axis with the blade leading edge

$z$	$R_T/3$	$2R_T/3$	$R_T$	$4R_T/3$	$5R_T/3$
$z$ (mm)	52.5	100	150	200	250
$\langle C_{\theta 2} \rangle$ (m.s <sup>-1</sup> )	5.32	6.38	6.23	5.87	5.62
$\sigma_{C_{\theta 2}}$ (m.s <sup>-1</sup> )	1.54	1.56	1.28	0.9	0.21

Table 4: *Tangential velocity for the EWT*

imatively equal to  $6^\circ$ . The BWT, designed with the classical classical blade-element/ momentum theory assumed any rotation in the wake, which is note in good agreement with the experimental results.

Axial velocity fields and profiles for the BWT are presented in Figs. 8b, 8d and 8f. Close to the wind turbine, at a distance  $z = R_T/3$ , the axial velocity is approximately constant and equal to 6 m.s<sup>-1</sup>. The associated axial induction factor is  $a = 0,4$ , that is higher to the design axial induction factor. Thus the fluid is more decelerated than it was predicted by the design specifications. The shapes of axial velocity profiles for the BWT presented in [Fig.8f] testified the continuous deceleration of the fluid in the wake of the BWT. As the distance  $z$  from the wind turbine increases, the shape of the axial velocity profiles become linear and for a given radial coordinate  $r$ , the axial velocity decreases. At  $r = 2R_T/3$ , the axial velocity decreases from 6 m.s<sup>-1</sup> for  $z = R_T/3$  to 4 m.s<sup>-1</sup> for of  $z = 5R_T/3$ . On the contrary, for the same radial coordinate  $r = 2R_T/3$  the axial velocity behind the EWT is approximately constant for various distance  $z$ .

For comparison of the two wind turbines the rotation of the fluid in the wake is much more significant with the EWT than with the BWT. The comparison of the wake angle show that the wake expansion is more significant with the BWT than with the EWT. Moreover, the EWT presents a higly stable wake compared to the BWT. Indeed, the full wake behind the EWT has an approximately constant axial velocity whereas the wake induces by the BWT is not evenly decelerated. As the distance  $z$  increased, the axial velocity profiles behind the BWT become linear and the deceleration of the fluid is spread to the full wake. It could be explained by the larger negative axial velocity near the hub of the BWT compared to the EWT that induced a higher axial velocity gradient. Moreover far from the wind turbine, the fluid is slower behind the BWT than behind the EWT. In addition, with the same design brief and a similar mechanical power produced, the EWT induces a higher rotating wake than the BWT and slow down less the fluid far from the wind turbine. Moreover, wake expansion is definitely enhanced by the BWT. The results of the stereo-PIV show a good correlation between the design brief of the EWT and the experimental results. Indeed, the tangential velocity and the axial induction factor are realy closed to the design values. In other words, the EWT performed how it was supposed to perform according to the method design.

$z$	$R_T/3$	$2R_T/3$	$R_T$	$4R_T/3$	$5R_T/3$
$z$ (mm)	52.5	100	150	200	250
$\langle C_{z2} \rangle$ (m.s <sup>-1</sup> )	6.61	6.24	6.66	6.47	6.70
$\sigma_{C_{z2}}$ (m.s <sup>-1</sup> )	0., 26	0.23	0, 21	0, 23	0.21
$\langle a \rangle$	0.339	0.376	0.334	0.353	0.330

Table 5: *Axial velocity and axial induction factor for EWT*

## 5. Conclusion

A 300 mm diameter wind turbine operating at a very low tip-speed ratio  $\lambda = 1$  has been designed with an innovative design method based on the Euler's turbomachinery theorem. It has been tested in wind tunnel and compared to a wind turbine designed according to the classical blade-element/ momentum theory in order to assess its performance. This wind turbine presents a power coefficient similar to the classical wind turbine but at a very low optimum tip-speed ratio. To the author's knowledge, it is the first centimeter-scale wind turbine that achieved such performance at tip-speed ratio  $\lambda = 1$ . The wind turbine presents a very low cut-in wind speed and generates high torque at low tip-speed ratio that makes it an efficient wind turbine for low wind speed applications. The wake analysis have shown that the wind turbine induced a stable and highly rotating wake compared to the classical wind turbine that could be useful to drive a contra-rotating rotor.

## References

- [1] Abhishiktha Tummala, Ratna Kishore Velamati, Dipankur Kumar Sinha, V. Indrajaya, and V. Hari Krishna. A review on small scale wind turbines. *Renewable and Sustainable Energy Reviews*, 56:1351–1371, 2016.
- [2] Ravi Anant Kishore and Shashank Priya. Design and experimental verification of a high efficiency small wind energy portable turbine (SWEPT). *Journal of Wind Engineering and Industrial Aerodynamics*, 118:12–19, 2013.
- [3] H. Glauert. *Airplane Propellers*. Springer Berlin Heidelberg, Berlin, Heidelberg, 1935.
- [4] Jens Nørkær Sørensen. *General Momentum Theory for Horizontal Axis Wind Turbines*, volume 4 of *Research Topics in Wind Energy*. Springer International Publishing, Cham, 2016.
- [5] A. Betz. *Windenergie und ihre Ausnützung durch Windmühlen*. Vandenhoeck and Ruprecht, Göttingen, 1926.
- [6] Tony Burton, David Sharpe, Nick Jenkins, and Ervin Bossanyi. *Wind Energy Handbook*. 2002.
- [7] N.E. Joukowsky. *Vortex theory of a rowing screw*. *Trudy Otdeleniya Fizicheskikh Nauk Obshchestva Lubitelei Estestvoznaniya*, volume 16(1). 1912.
- [8] D. H. Wood. Maximum wind turbine performance at low tip speed ratio. *Journal of Renewable and Sustainable Energy*, 7(5):053126, 2015.
- [9] Jorge Elizondo, Jaime Martínez, and Oliver Probst. Experimental study of a small wind turbine for low- and medium-wind regimes. *International Journal of Energy Research*, 33(3):309–326, 2009.
- [10] Maryam Refan and Horia Hangan. Aerodynamic Performance of a Small Horizontal Axis Wind Turbine. *Journal of Solar Energy Engineering*, 134(021013), 2012.
- [11] Ronit K. Singh and M. Rafiuddin Ahmed. Blade design and performance testing of a small wind turbine rotor for low wind speed applications. *Renewable Energy*, 50:812–819, 2013.

- [12] João P. Monteiro, Miguel R. Silvestre, Hugh Piggott, and Jorge C. André. Wind tunnel testing of a horizontal axis wind turbine rotor and comparison with simulations from two Blade Element Momentum codes. *Journal of Wind Engineering and Industrial Aerodynamics*, 123:99–106, 2013.
- [13] Meng-Hsien Lee, Y.C. Shiah, and Chi-Jeng Bai. Experiments and numerical simulations of the rotor-blade performance for a small-scale horizontal axis wind turbine. *Journal of Wind Engineering and Industrial Aerodynamics*, 149:17–29, 2016.
- [14] Salih N. Akour, Mohammed Al-Heydari, Talha Ahmed, and Kamel Ali Khalil. Experimental and theoretical investigation of micro wind turbine for low wind speed regions. *Renewable Energy*, 116:215–223, 2018.
- [15] Ali M. Abdelsalam, W.A. El-Askary, M.A. Kotb, and I.M. Sakr. Experimental study on small scale horizontal axis wind turbine of analytically-optimized blade with linearized chord twist angle profile. *Energy*, 216:119304, 2021.
- [16] Yasuyuki Nishi, Yusuke Yamashita, and Terumi Inagaki. Study on the rotor design method for a small propeller-type wind turbine. *Journal of Thermal Science*, 25(4):355–362, 2016.
- [17] Hiroyuki Hirahara, M. Zakir Hossain, Masaaki Kawahashi, and Yoshitami Nonomura. Testing basic performance of a very small wind turbine designed for multi-purposes. *Renewable Energy*, 30(8):1279–1297, 2005.
- [18] Ravi Anant Kishore, Anthony Marin, and Shashank Priya. Efficient Direct-Drive Small-Scale Low-Speed Wind Turbine. *Energy Harvesting and Systems*, 1(1-2):27–43, 2014.
- [19] Fabio Mendonca and Joaquim Azevedo. Design and power production of small-scale wind turbines. In *2017 International Conference in Energy and Sustainability in Small Developing Economies (ES2DE)*, pages 1–6, Funchal, Portugal, 2017. IEEE.
- [20] Yung-Jeh Chu and Heung-Fai Lam. Comparative study of the performances of a bio-inspired flexible-bladed wind turbine and a rigid-bladed wind turbine in centimeter-scale. *Energy*, 213:118835, 2020.
- [21] Fujun Xu, Fuh-Gwo Yuan, Lei Liu, Jingzhen Hu, and Yiping Qiu. Performance Prediction and Demonstration of a Miniature Horizontal Axis Wind Turbine. *Journal of Energy Engineering*, 139(3):143–152, 2013.
- [22] David Rancourt, Ahmadreza Tabesh, and Luc Fréchette. Evaluation of centimeter-scale micro wind mills: Aerodynamics and electromagnetic power generation. *Proc. PowerMEMS*, pages 93–96, 2007.
- [23] M. Perez, S. Boisseau, P. Gasnier, J. Willemin, M. Geisler, and J. L. Reboud. A cm scale electret-based electrostatic wind turbine for low-speed energy harvesting applications. *Smart Materials and Structures*, 25(4):045015, 2016. Publisher: IOP Publishing.
- [24] Mohamed Y. Zakaria, Daniel A. Pereira, and Muhammad R. Hajj. Experimental investigation and performance modeling of centimeter-scale micro-wind turbine energy harvesters. *Journal of Wind Engineering and Industrial Aerodynamics*, 147:58–65, 2015.
- [25] D A Howey, A Bansal, and A S Holmes. Design and performance of a centimetre-scale shrouded wind turbine for energy harvesting. *Smart Materials and Structures*, 20(8):085021, 2011.
- [26] P. Giguère and M. S. Selig. New Airfoils for Small Horizontal Axis Wind Turbines. *Journal of Solar Energy Engineering*, 120(2):108–114, 1998.
- [27] Haseeb Shah, Jasir Kitaba, Sathyajith Mathew, and Chee Lim. Experimental Flow Visualization over a Two-Dimensional Airfoil at Low Reynolds Number. 2014.
- [28] Philippe Giguère and Michael S. Selig. Low Reynolds Number Airfoils for Small Horizontal Axis Wind Turbines. *Wind Engineering*, 21(6):367–380, 1997.
- [29] P B S Lissaman. Low-Reynolds-Number Airfoils. *Annual Review of Fluid Mechanics*, 15(1):223–239, 1983.
- [30] D. J. Sharpe. A general momentum theory applied to an energy-extracting actuator disc. *Wind Energy*, 7(3):177–188, 2004.
- [31] Dennis Leung, Y. Deng, and Michael K.H. Leung. Design optimization of a cost-effective micro wind turbine. *WCE 2010 - World Congress on Engineering 2010*, 2:988–993, 2010.
- [32] Matthew M. Duquette, Jessica Swanson, and Kenneth D. Visser. Solidity and Blade Number Effects on a Fixed Pitch, 50 W Horizontal Axis Wind Turbine. *Wind Engineering*, 27(4):299–316, 2003.
- [33] M.S. Selig. *Summary of Low Speed Airfoil Data*. Number vol. 2 in Summary of Low Speed Airfoil Data. SoarTech Publications, 1995.
- [34] M. Raffel, Christian Willert, and Juergen Kompenhans. *Particle Image Velocimetry: A Practical Guide*. 1998.